Journal of Molecular Structure 1231 (2021) 130023

Contents lists available at ScienceDirect

Journal of Molecular Structure

journal homepage: www.elsevier.com/locate/molstr

Removal of volatile organic compounds from air using supported ionic liquid membrane containing ultraviolet-visible light-driven Nd-TiO_2 nanoparticles

Jinlong Li[a,b,*], Boxin Li[a], Guozhe Sui[a,b,*], Lijuan Du[a], Yan Zhuang[a], Yulin Zhang[a], Yuanfang Zou[a]

[a] *College of Chemistry and Chemical Engineering, Qiqihar University, Qiqihar 161006, P. R. China*
[b] *Heilongjiang Provincial Key Laboratory of Catalytic Synthesis for Fine Chemicals, Qiqihar University, Qiqihar 161006, P. R.China*

ARTICLE INFO

Article history:
Received 27 December 2020
Revised 20 January 2021
Accepted 24 January 2021
Available online 29 January 2021

Keywords:
Photocatalytic membrane-based reactor
Volatile organic compounds
Supported ionic liquid membrane
Photocatalytic reaction

ABSTRACT

Volatile organic compounds (VOCs) with toxicity properties discharged from industrial emissions and combustion engines threaten human health and cause environmental problems. Therefore, it is important to develop technologies to remove VOCs from air. In this study, the performance of Nd (neodymium) -TiO_2 nanoparticles embedded in a supported ionic liquid membrane (SILM) for removal of VOCs from air was investigated. Aiming at functionalizing the ionic liquid membrane with photocatalytic capability, we developed a facile and effective approach for the removal of VOCs by coupling highly efficient photocatalysts with the SILM. Nd-TiO_2 nanoparticles, which are ultraviolet-visible (UV–Vis) light-driven photocatalysts, were prepared by sol-gel and immersed in the SILM for use as a photocatalytic membrane-based reactor. The gaseous VOCs tested were toluene, acetone, chloroform, benzene, and xylene. We confirmed that at a loading of 50 wt% Nd-TiO_2 nanoparticles (1 wt% Nd content) and 1-hexyl-3-methylimidazolium hexafluorophosphate ([HMI*m*]PF_6) as SILM ([HMI*m*]PF_6/Nd-TiO_2 SILM), the as-prepared photocatalytic membrane-based reactor exhibited higher removal efficiency of VOCs from air (60~80% removal after 10 h) under UV–Vis light illumination than individual SILM or photocatalytic systems. Effluent gas analysis revealed that 25–55% of VOCs was decomposed and mineralized in the photocatalytic membrane reactor, which exhibited higher VOCs removal efficiency than membrane separation. These results indicate that the photocatalytic membrane-based reactor containing Nd-TiO_2 nanoparticles and SILM designed in this study is highly active and stable. This study on [HMIm]PF_6/Nd-TiO_2 SILM was initiated to couple membrane separation with photocatalytic degradation of gaseous VOCs and can serve as a promising way for eliminating harmful VOCs with low concentration from air.

1. Introduction

Volatile organic compounds, also known as VOCs, refer to the organic chemical compounds with significant saturated vapor pressure (>70 Pa at normal temperature) and boiling points within the range of 50–260 °C at normal pressure [1], mainly include hydrocarbons, benzenes, organic chlorides, aldehydes, ketones, and fatty acids [2]. These VOCs, principally discharged from industrial emissions and combustion engines, generally have high-risk biological toxicity properties, which threaten human health. In addition, these VOCs will directly or indirectly cause environmental problems such as haze and photochemical smog, which pose a global environmental issue [3]. Therefore, to control the concentration of VOC pollutants, the technology of VOC abatement has become a research topic of interest in recent years. However, conventional techniques are less efficient at handling low concentrations of VOC [4]; therefore, new techniques are needed to degrade VOCs present at low concentration.

Photocatalytic technology is the optimal strategy for VOC abatement, because it can mineralize VOCs to fewer polluting substances by efficient utilization of light energy [5]. Furthermore, it is one of the most effective treatments to remove gaseous VOCs with low concentration due to its efficiency and energy-saving advantage at normal temperature [6]. Therefore, many catalysts with high photoactive performance are being developed to degrade gaseous VOCs from air. Among them, TiO_2 has been widely used owing to its good stability and low toxicity in controlling pollution [7]. However, TiO_2 has two obvious drawbacks: (1) the efficiency of

---

* Corresponding authors.
E-mail addresses: jinlong@qqhru.edu.cn (J. Li), gzhsui@qqhru.edu.cn (G. Sui).

https://doi.org/10.1016/j.molstruc.2021.130023

natural sunlight utilization is low because it can only absorb near-ultraviolet light caused by wide forbidden band width (~3.2 eV) [8]; (2) the photocatalytic efficiency is reduced due to rapid recombination of photogenerated electron-hole pairs [9]. Therefore, much research attention has been devoted to the improvement of the photocatalytic activity of TiO_2 by modifications, such as doping of metal or non-metal, and morphological modification [10].

In recent publications, rare earth metals have been proved to be one of the most efficient dopants for effectively preventing the recombination of photogenerated electron-hole pairs and extending the range of response spectrum [11]. As a conventional doping metal, Nd exhibited higher photocatalytic performance and utilization of light energy due to the 4f electron transition in rare earth metals [12]. Alam et al. [13] synthesized Nd-V-ZnO with spindle-like shape by using an ultrasonic-assisted sol-gel method, and the doping of Nd and V metals enhanced the degradation efficiency of aqueous organic pollutants under visible light. Wang et al. [14] deposited Nd and TiO_2 on SBA-15 substrate with mesoporous structure, and the obtained Nd-TiO_2-SBA-15 showed high photoactive and good acid-base adaptability for methyl orange in the pH range of 2–10. Nd-doped TiO_2 can increase the adsorption capacity of the catalyst surface, thus improving the photocatalytic activity [15]. However, research about gaseous VOCs abatement using Nd-doped oxide semiconductor has been less reported, especially for removing gaseous VOCs with low concentration. Therefore, the technology of photocatalysis is usually coupled with other technologies to improve the efficiency of gaseous VOC removal.

Membrane separation technology has been widely used in the separation of VOCs because of its high recovery and high efficiency [16]. Comparing with conventional polymeric membranes, supported liquid membranes exhibit higher VOC permeability and selectivity due to the properties of the liquid solvent. According to the facilitated transport theory, ionic liquids are promising, offering higher VOC permeability and selectivity due to their thermal stability and low volatility [17, 18]. Wang et al. [19] reviewed the recent applications of supported ionic liquid membranes (SILMs) for VOCs separation and stated the transport mechanisms of organic compounds. Uragami et al. [20] reported the separation performance of the poly(styrene)-b-poly(dimethylsiloxane) membranes containing 1-allyl-3-butylimidazilium bis (trifluoromethane sulfonyl) imide ([ABIM]TFSI) for removing chloroform, benzene, and toluene from aqueous solutions. The authors revealed that [ABIM]TFSI plays an important role as an absorbent to selectively separate VOCs from the aqueous solution. Dahi et al. [21] prepared SILMs by immobilizing [C(4)C(1)im][BF4] in a porous Matrimid membrane. The prepared SILMs showed better performance of separation of VOCs, such as ethanol and cyclohexane, from the solution due to the best sorption capacities and the good sorption selectivity of [C(4)C(1)im][BF4] for VOCs. However, most studies only focus on VOCs separation in the liquid phase, and the investigations on the separation of gaseous VOCs (such as benzene, toluene, and formaldehyde) with low concentration from air are much scarce. Furthermore, the gaseous VOCs separated using membrane technology cannot be degraded into nontoxic CO_2 and H_2O through its physical process. It is therefore necessary to develop and study a typical membrane process coupled with other treatment technology to improve the elimination performance of harmful VOCs from air.

In this study, we present the detailed study of the VOC removal performance of a coupled process of SILM and photocatalysis based on 1-hexyl-3-methylimidazolium hexafluorophosphate ([HMI*m*]PF_6) and Nd-TiO_2 nanoparticles ([HMI*m*]PF_6/Nd-TiO_2 SILM). Particularly, this study focused on the synergistic effect of [HMIm]PF_6/Nd-TiO_2 SILM, i.e., the concentration of [HMIm]PF_6 SILM and photocatalytic action of Nd-TiO_2. Toluene (C_7H_8), acetone (C_3H_6O), benzene (C_6H_6), xylene (C_8H_{10}), and chloroform ($CHCl_3$) single-gas and multiple-gas removal performances of [HMIm]PF_6/Nd-TiO_2 SILM were investigated under visible light illumination, and the mechanism underlying the removal of gaseous VOCs was discussed. We also investigated the effects of operation conditions on the removal performance, and the experimental results were correlated to the variation of the operation conditions.

2. Experimental

2.1. Materials

Tetrabutyl titanate ($C_{16}H_{36}O_4Ti$) was selected as the Ti source to prepare TiO_2, glacial acetic acid (CH_3COOH) was used as a hydrolysis inhibitor of tetrabutyl titanate, nitric acid (HNO_3) was used to adjust the solution pH, neodymium nitrate ($Nd(NO_3)_3 \bullet 6H_2O$) was the source of metal Nd, and absolute ethanol (CH_3CH_2OH) was used as solvent. Toluene (C_7H_8), acetone (C_3H_6O), benzene (C_6H_6), xylene (C_8H_{10}), and chloroform ($CHCl_3$) were chosen as gaseous VOC samples for the removal experiment. The ionic liquid used was 1-hexyl-3-methylimidazolium hexafluorophosphate ([HMI*m*]PF_6). The chemicals were purchased from Aladdin Chemistry Co. Ltd. and were of analytical grade and were used without purification. Polyvinylidene fluoride film (PVDF) with 95 μm of thickness, 0.1 μm of mean pore size, and 70% porosity was provided by Millipore Co. Ltd. The deionized water used in this experiment was produced from a UPE-60 water purification equipment.

2.2. Preparation of Nd-TiO_2 nanoparticles

The Nd-TiO_2 nanoparticles were synthesized via a sol-gel method: 2 mL of $C_{16}H_{36}O_4Ti$ was dissolved in 9.8 mL of CH_3CH_2OH, to which 2 mL of CH_3COOH was further added during stirring. The pH of the mixture was adjusted to ~3 by adding HNO_3, and the mixture was stirred vigorously for 1 h to form solution A. Next, an appropriate amount of $Nd(NO_3)_3 \cdot 6H_2O$, which was varied according to the intended mass ratio of Nd:TiO_2 (0, 0.5, 0.8, 1.0, and 1.5% (wt%)), was added in the deionized water and stirred continuously until dissolved, and the obtained solution was labeled as solution B. Solution B was slowly added to solution A at the dropping rate of 1 mL min^{-1}, and the resulting solution was kept under continuous stirring for 24 h at 40 °C. The gel was formed after aging in air for 48 h and then dried at 60 °C for 10 h and washed with deionized water several times. The final Nd-TiO_2 nanoparticles were obtained after calcination in an air furnace at 550 °C for 2 h at a heating rate of 5 °C min^{-1}.

2.3. Preparation of SILM

A flat membrane module with membrane area of 0.065 m^2 was used for the VOCs removal measurement. The PVDF membrane was on the porous polypropylene plate, which was used as permeated gas transport channel. The detailed construction of the flat membrane module is described in our previous report [22]. [HMIm]PF_6 (2.5 g) and Nd-TiO_2 nanoparticles (0.2 g) were mixed completely, and were then uniformly distributed onto the hydrophilic surface of the PVDF supported membrane treated with corona discharge. Some [HMIm]PF_6 was spread on this top hydrophilic surface with a wetting tension of 70 mN/m and then soaked into the pores of PVDF membrane [22]. The other surface of PVDF hydrophobic bottom layer will support the top [HMIm]PF_6 liquid layer, due to the hydrophilic-hydrophobic interaction between the liquid and the surface of PVDF membrane. A [HMIm]PF_6/Nd-TiO_2 SILM was obtained and was durable under a transmembrane pressure up to 2–3 atm. The membrane thickness of the obtained [HMIm]PF_6/Nd-TiO_2 SILM was ~20 μm, as estimated from the quality of the used [HMIm]PF_6.

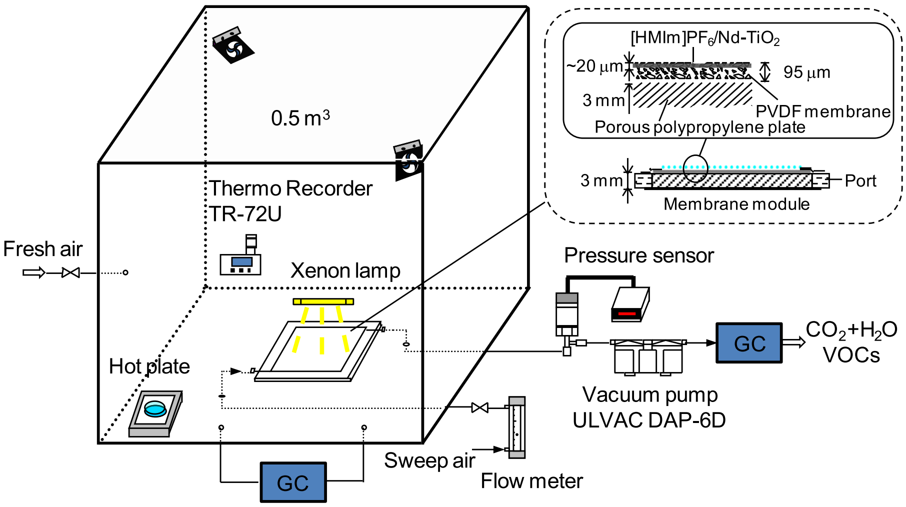

Fig. 1. Membrane catalytic diagram for removing VOCs.

2.4. Characterization of Nd-TiO$_2$ nanoparticles

X-ray diffraction (XRD) analysis was performed over the 2θ range of 10–80 ° by using the D8 X-ray diffractometer (Bruker-AXS, Germany). Fourier transform infrared (FT-IR) spectra were acquired using the Nexus 670 infrared spectrometer (Nicolet, USA). UV-Visible diffuse-reflectance spectra (UV–Vis DRS) were measured on Lamda 35 UV–Vis spectrophotometer (PE, USA), using BaSO$_4$ as a reflectance standard. X-ray photoelectron spectroscopy (XPS) analysis was performed on ESCALAB250Xi X-ray photoelectron spectrometer (Thermo, USA). Scanning electron microscopy (SEM) images were recorded on the S-3400 scanning electron microscope (Hitachi, Japan), and transmission electron microscopy (TEM) images were acquired with the H-7650 transmission electron microscope (Hitachi, Japan). The specific surface area was analyzed using the Nova 2000e N$_2$ adsorption-desorption apparatus (Quantachrome, USA) in the relative pressure ranging of 0.05–0.35.

2.5. VOCs removal measurement

Gaseous VOCs removal from air was conducted, in a 0.5 m^3 black chamber with Teflon film coating to avoid VOC adsorption (Fig. 1). The air containing VOCs in the chamber was mixed completely by horizontal and vertical fans. The experimental apparatus comprised a SILM membrane module and a 500 W xenon lamp with a light length cut-off filter (<420 nm or >420 nm) placed in the chamber, diaphragm vacuum pumps (DAP-6D, ULVAC, Japan), a hot plate, a gas chromatography (GC) system (SP-6890, Lunan-RUIHONG, China), pressure sensors, and a 500 W xenon lamp. A certain amount of liquid VOCs, calculated through the determined room temperature and atmospheric pressure, was injected onto the hot plate in the chamber and then vaporized to gaseous VOCs to achieve the set concentration of 1 000 ppm. When the liquid VOCs were vaporized completely, the concentration in the chamber was determined by the GC with a hydrogen flame detector (FID). The membrane system was operated using a diaphragm vacuum pump and a needle valve. The pressure at the permeate side of the membrane module was maintained at 10 kPa and the sweep air flow rate was controlled at 0.5 L min^{-1}, they were detected using a pressure sensor and a flowmeter, respectively. After operating for 30 min in the dark, the adsorption-desorption equilibrium of gaseous VOCs on the [HMIm]PF$_6$/Nd-TiO$_2$ SILM was achieved and then a 500 W xenon lamp, with a light length cut-off filter, was turned on to the membrane module. The gaseous VOCs was concentrated on the surface of [HMIm]PF$_6$/Nd-TiO$_2$ SILM under the difference of VOCs partial pressure, and most of which was degraded to CO$_2$ and H$_2$O by Nd-TiO$_2$ under visible light illumination. Meanwhile, a little gaseous VOCs and the degradation products permeated the [HMIm]PF$_6$/Nd-TiO$_2$ SILM into the permeate side of membrane module according to the solution-diffusion mechanism. The composition and concentration of VOCs in the chamber and at the outlet of the membrane module were measured by GC with a hydrogen flame detector (FID) and a thermal conductivity detector (TCD), respectively. In addition, the photocatalytic degradation efficiency of VOCs was calculated by measuring the concentration of CO$_2$ in the membrane permeate stream. To prevent negative pressure in the chamber, fresh air could be supplied through the inlet settled at the wall of the chamber.

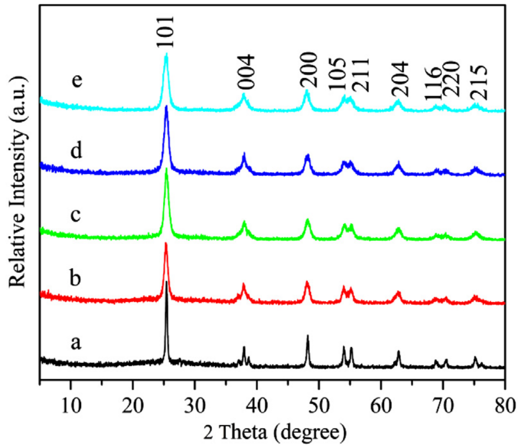

Fig. 2. XRD patterns of (a) TiO$_2$, (b) 0.5 wt% Nd-TiO$_2$, (c) 0.8 wt% Nd-TiO$_2$, (d) 1.0 wt% Nd-TiO$_2$, and (e) 1.5 wt% Nd-TiO$_2$.

3. Results and discussion

3.1. Characterization

The XRD patterns of TiO$_2$ and Nd-TiO$_2$ nanoparticles with different contents of Nd are shown in Fig. 2. All Nd-TiO$_2$ nanoparticles exhibited XRD profiles similar to that of TiO$_2$, which shows diffraction peaks at 2θ of 25.3°, 37.9°, 48.1°, 54.0°, 55.1°, 62.7°, 68.8°, 70.5°, and 75.4° that correspond to the anatase (101), (004), (200), (105), (211), (204), (116), (220), and (215) lattice planes

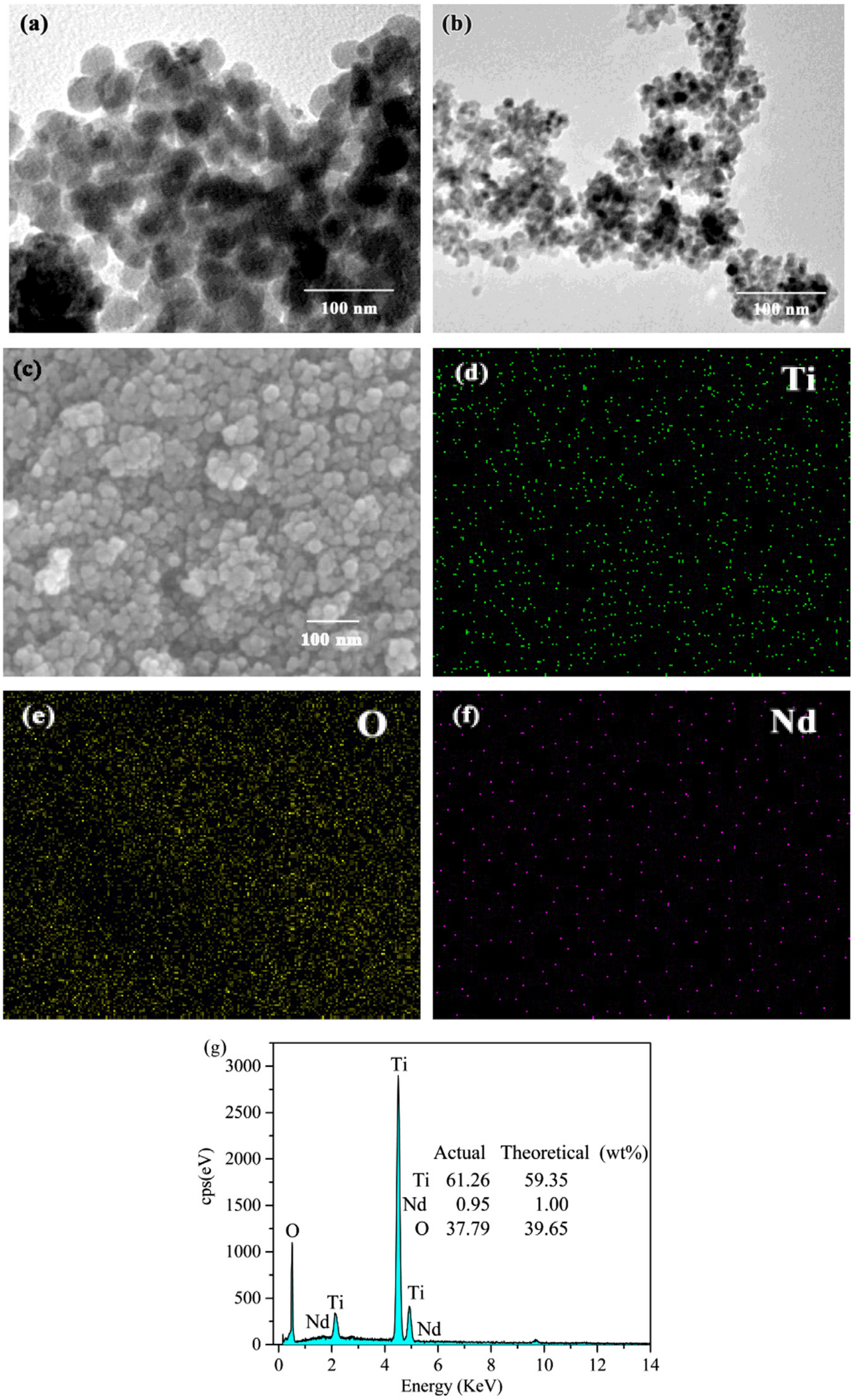

	Actual	Theoretical (wt%)
Ti	61.26	59.35
Nd	0.95	1.00
O	37.79	39.65

Fig. 3. TEM images of (a) pure TiO_2, (b) 1 wt% Nd-TiO_2, SEM image of (c) 1 wt% Nd-TiO_2, elemental maps of (d) Ti atoms, (e) O atoms, and (f) Nd atoms, and (g) EDS spectra of 1 wt% Nd-TiO_2.

(JCPDS card no. 21–1272), respectively. This indicated that other crystal forms of TiO_2 were not formed during preparing Nd-TiO_2 nanoparticles. The ionic radius of Nd^{3+} (0.104 nm) is larger than Ti^{4+} (0.088 nm) [23], therefore, Nd^{3+}cannot replace Ti^{4+} in the lattice, but in the state of Nd_2O_3, it may be adsorbed on the surface of TiO_2. However, there was no characteristic diffraction peak of Nd_2O_3 at $2\theta = 32.5°$ [24] because the doping amount of Nd was low. It can be seen from the figure that the full width half-maximum (FWHM) of the catalysts becomes larger after doping Nd. The average crystallite size (D) of Nd-TiO_2 nanoparticles, which was calculated from the Scherrer equation based on the FWHM of (101) XRD peak, decreased as shown in Table 1, indicating that the specific surface area of Nd-TiO_2 nanoparticles may be increased by Nd doping [25].

TEM and SEM images of pure TiO_2 and Nd-TiO_2 nanoparticles, and the elemental maps of Ti, O and Nd in 1.0 wt% Nd-TiO_2 are shown in Fig. 3. All the prepared catalysts showed a spherical or globular particle shape and a slight agglomeration. The average particle size of pure TiO_2 was ca. 40 nm, whereas the average particle size of Nd-TiO_2 nanoparticles was reduced to 15–20 nm.

Table 1
Pore size, specific surface area and average anatase crystallite size parameters of TiO_2 and Nd-TiO_2.

Sample	Pore Diameter (nm)	Surface Area ($m^2\ g^{-1}$)	Anatase Crystallite Size (nm)
TiO_2	7.23	45.34	21.53
Nd-TiO_2(0.5 wt%)	6.56	105.82	13.72
Nd-TiO_2(0.8 wt%)	6.57	130.62	12.24
Nd-TiO_2(1.0 wt%)	6.59	150.27	12.22
Nd-TiO_2(1.5 wt%)	6.57	129.83	11.57

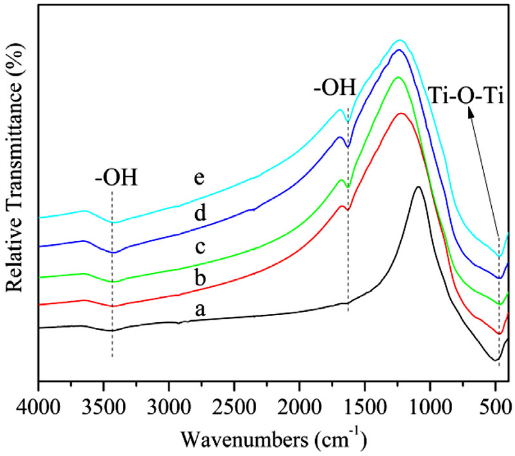

Fig. 4. FT-IR spectra of (a) TiO_2, (b) 0.5 wt% Nd-TiO_2, (c) 0.8 wt% Nd-TiO_2, (d) 1.0 wt% Nd-TiO_2, and (e) 1.5 wt% Nd-TiO_2.

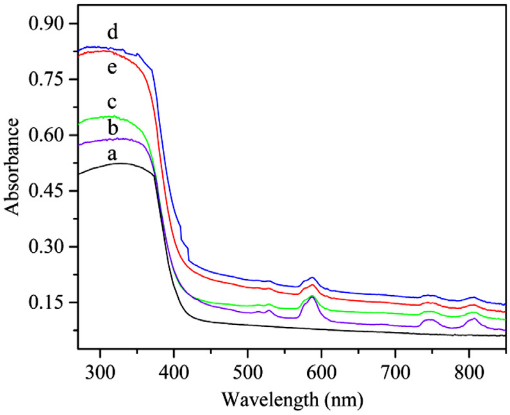

Fig. 5. UV–Vis diffuse reflectance spectra of (a) TiO_2, (b) 0.5 wt% Nd-TiO_2, (c) 0.8 wt% Nd-TiO_2, (d) 1.0 wt% Nd-TiO_2, and (e) 1.5 wt% Nd-TiO_2.

This indicated that the growth of the catalyst grains can be effectively suppressed by the doping of Nd. This reduction of the particle size can increase the specific surface area of Nd-TiO_2 nanoparticles, which caused a further increase of the photocatalytic activity. Fig. 3(d-f) show that the elements of Ti, O, and Nd are dispersed uniformly in 1.0 wt% Nd-TiO_2 nanoparticles. Fig. 3(g) shows that the actual contents of Ti, Nd, and O correspond to 61.26 wt%, 0.95 wt%, and 37.79 wt%, respectively, which are consistent with the theoretical contents in Nd-TiO_2 nanoparticles. The difference between the actual content and the theoretical content can be attributed to instrument error.

FT-IR spectra of TiO_2 and Nd-TiO_2 nanoparticles are shown in Fig. 4. The wide absorption bands observed over the range of 450–800 cm^{-1} were assigned to the stretching mode of Ti-O bond and the bridging mode of Ti-O-Ti bond, which are characteristic peaks of TiO_2 [26]. Notably, the Ti-O or Ti-O-Ti bonds in Nd-TiO_2 nanoparticles were significantly red-shifted, which might have been caused by the doping of Nd. The absorption peak at 1623 cm^{-1} and the broad absorption peak at 3425 cm^{-1} were attributed to the bending and stretching vibrations of O–H, which are related to water adsorbing on the surface of the catalyst [27]. Compared with pure TiO_2, the absorption peak at 3425 cm^{-1} became stronger with increasing of Nd doping quantity. This indicated that the Nd dopant enhances water adsorption resulting in more hydroxyl radicals, increasing the photocatalytic performance of Nd-TiO_2 [28].

DRS spectra of TiO_2 and Nd-TiO_2 nanoparticles are shown in Fig. 5. Compared with pure TiO_2, the absorption spectra of Nd-TiO_2 nanoparticles showed an obvious red shift extended to the visible light region. This was due to the charge transfer transition between the dopant electrons of Nd and the TiO_2 conduction band [29], indicating that the light absorption capacity of the catalyst was greatly improved [30]. Furthermore, three absorption bands appeared in the spectra of Nd-TiO_2 nanoparticles as the reference of $Nd(NO_3)_3$ DRS spectra, which was attributed to the 4f transition of Nd(III) ions. By varying the content of Nd, the absorption capacity of Nd-TiO_2 nanoparticles under visible light illumination was different, and Nd-TiO_2 nanoparticles with 1.0 wt% of Nd exhibited strong visible light absorption.

N_2 adsorption-desorption isotherms and the corresponding pore size distribution curves of pure TiO_2 and Nd-TiO_2 (1.0 wt%)

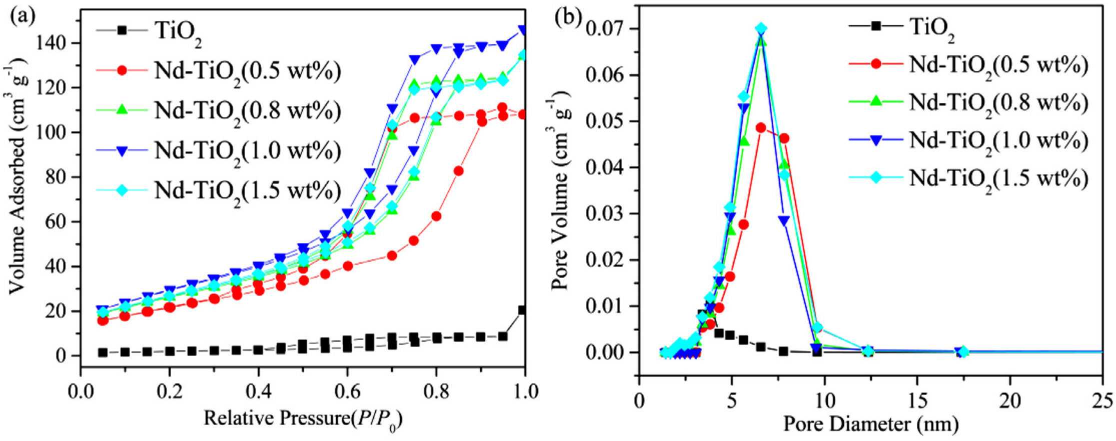

Fig. 6. (a) N_2 adsorption-desorption isotherms and (b) pore size distribution curves of TiO_2 and Nd-TiO_2 nanoparticles.

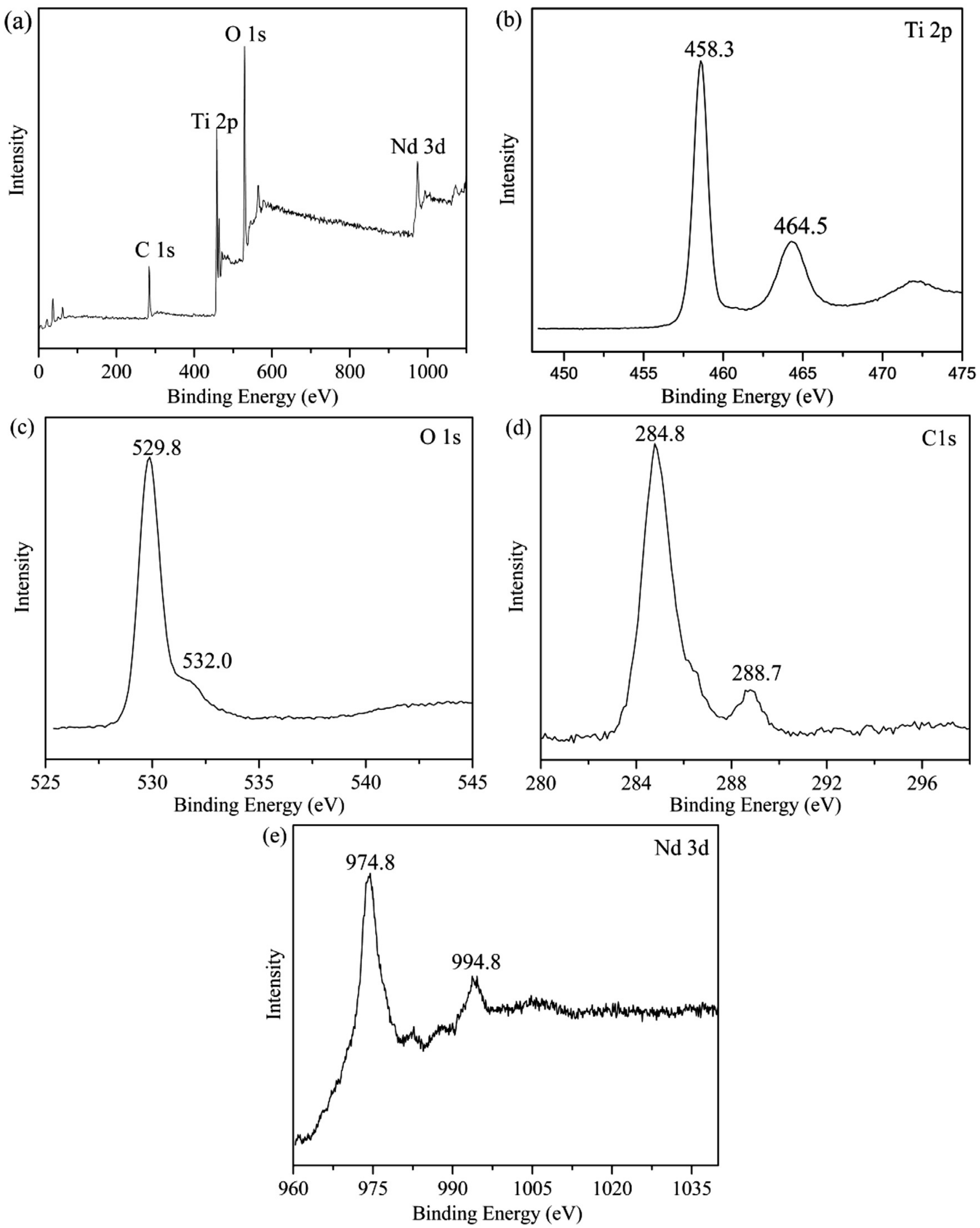

Fig. 7. (a) Overview of the XPS spectra and individual high-resolution XPS spectra for (b) Ti 2p, (c) O 1 s, (d) C 1 s, and (e) Nd 3d of Nd-TiO_2 (1.0 wt%) naoparticles.

nanoparticles are illustrated in Fig. 6. Table 1 shows the pore size and specific surface area parameters of the various component catalysts. According to the IUPAC classification, the adsorption-desorption isotherms of samples with an H1 hysteresis loop are all type IV curves [31], which indicate the presence of a mesoporous structure in the samples. The specific surface area and average pore size of all samples are summarized in Table 1. The specific surface area was 45.34, 105.82, 130.62, 150.27, and 129.83 m^2 g^{-1}, and the average pore size was 7.23, 6.56, 6.57, 6.57, 6.59, and 6.57 nm for pure TiO_2, 0.5 wt% Nd-TiO_2, 0.8 wt% Nd-TiO_2, 1.0 wt% Nd-TiO_2, and 1.5 wt% Nd-TiO_2, respectively. The specific surface area of Nd-TiO_2 nanoparticles increased with increasing Nd content, reaching a maximum when the amount of Nd was 1.0 wt%. Large specific surface area of the catalyst can provide more reactive centers, increasing the photocatalytic activity of the catalyst [32].

XPS spectra were measured to analyze the chemical states of Nd-TiO_2 (1.0 wt%) nanoparticles as shown in Fig. 7. Fig. 7(a) summarizes the XPS spectra of Nd-TiO_2 (1.0 wt%) nanoparticles, which contained four elements of Ti, O, C and Nd, with the binding energies of 284.1 eV, 458.1 eV, 529.1 eV, and 974.1 eV corresponding to C 1 s, Ti 2p, O 1 s and Nd 3d, respectively. As shown in Fig. 7(b), two main peaks were observed at 458.3 eV and 464.5 eV, which corresponded to Ti2p 3/2 and Ti2p 1/2 split peaks. This indicates that the Ti element exists as Ti^{4+} in the samples [33, 34].

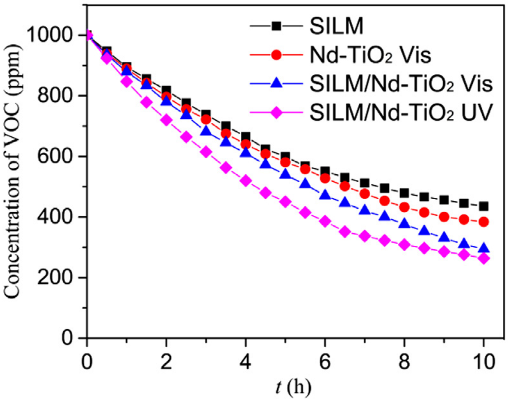

Fig. 8. Removal performance of toluene under different methods.

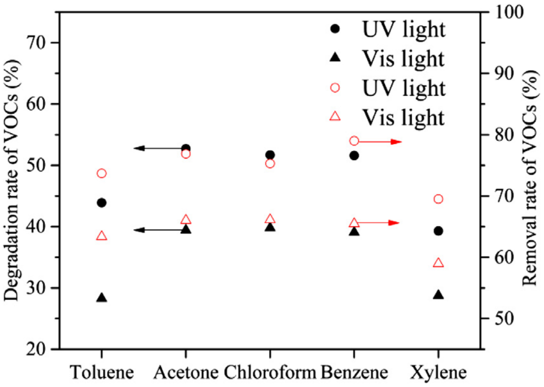

Fig. 10. Degradation rate and removal rate of VOCs by [HMIm]PF_6/Nd-TiO_2 SILM under UV light and visible light illumination for 10 h.

However, these peaks shifted slightly to a higher region of binding energy because the variation in the chemical state was caused by adding Nd in TiO_2. The O1s spectrum in Fig. 7(c) shows two peaks at 529.8 eV and 532.0 eV corresponding to the lattice oxygen and the oxygen from the surface-adsorbed O–H, respectively. In Fig. 7(d), the peak at 284.8 eV was attributed to surface impurity indefinite carbon ($C = C$ bonds), whereas the peak at 288.7 eV was assigned to C–O–Ti, disclosing that some carbon atoms substituted titanium atoms in the TiO_2 lattice [35]. In Fig. 7(e), the peaks of binding energy at 974.8 eV and 994.8 eV were attributed to Nd3d 5/2 and Nd3d 3/2, respectively, indicating that Nd exists as the form of Nd^{3+} in the TiO_2 lattice.

3.2. VOC removal performance

Performing removal of VOCs were measured using only membrane ([HMI*m*]PF_6 SILM) separation, photocatalysis (Nd-TiO_2) under visible light, and membrane ([HMI*m*]PF_6/Nd-TiO_2 SILM) catalytic separation under UV light and under visible light. The experimental results of toluene are shown in Fig. 8. All removal methods showed similar exponential reduction curves of toluene concentration in the chamber. The half reduction time of membrane separation, photocatalysis under visible light, and membrane catalytic separation under UV light and under visible light was 7.2 h, 6.5 h, 5.7 h, and 4.2 h, respectively. For only membrane ([HMI*m*]PF_6 SILM) separation processes, toluene was concentrated on the membrane surface, dissolved in [HMIm]PF_6 ionic liquid, and transported through the [HMIm]PF_6 membrane according to the solution-diffusion mechanism. Therefore, the membrane separation process exhibited the worst performance of removal of toluene compared with other separation methods. However, adding Nd-TiO_2 nanoparticles showed enhanced removal performance: the half reduction time under UV light and visible light was 3.0 h and 1.5 h shorter than membrane separation. This was because toluene was enriched on the membrane surface through membrane separation and was degraded into CO_2 and H_2O by Nd-TiO_2 nanoparticles under UV and visible light illumination. This synergistic effect between membrane separation and photocatalysis accelerated the rate of toluene removal through [HMIm]PF_6/Nd-TiO_2 SILM under light illumination.

The process of [HMIm]PF_6/Nd-TiO_2 SILM under UV and visible light illumination was further tested to evaluate the removal of other gaseous VOCs, such as acetone, chloroform, benzene, and xylene, and the experimental results are shown in Fig. 9. The variation of VOC concentration in the chamber was like that of toluene, and the photocatalytic membrane reaction process containing [HMIm]PF_6/Nd-TiO_2 SILM exhibited high performance for the removal of many types of VOCs. This indicated that the photocatalytic membrane reaction process can remove VOCs with low concentration. In addition, the removal efficiency under UV light was higher than that under visible light: for toluene, acetone, chloroform, benzene, and xylene, the half reduction time was 4.2 h, 4.0 h, 3.8 h, 3.9 h, and 5.0 h under UV light, respectively, whereas the half reduction time was 5.7 h, 6.0 h, 5.7 h, 5.2 h, and 6.5 h un-

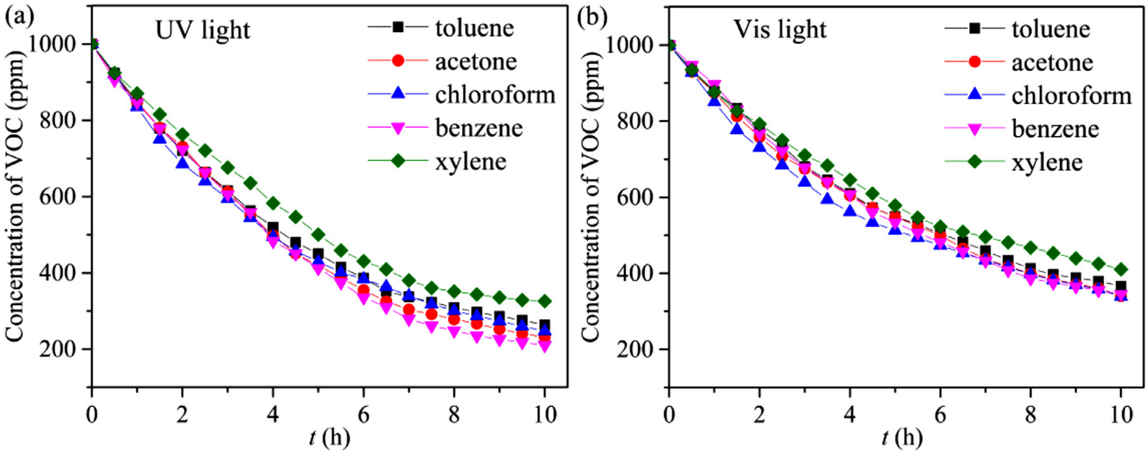

Fig. 9. Removal performance of VOCs by [HMIm]PF_6/Nd-TiO_2 SILM under (a) UV light and (b) visible light illumination.

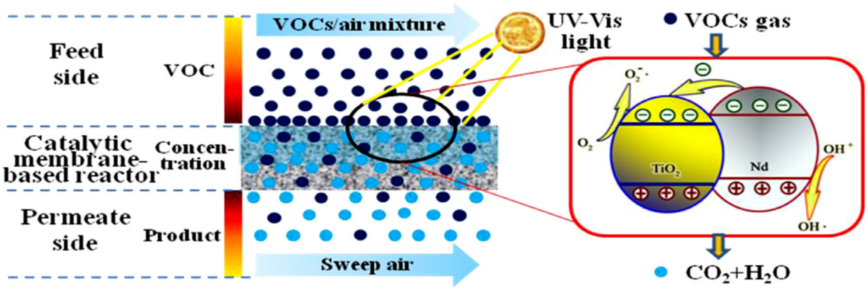

Fig. 11. Catalytic membrane-based mechanism diagram of VOCs removal through [HMIm]PF_6/Nd-TiO_2 SILM under UV light and visible light illumination.

der visible light, respectively. This was because the absorbance of Nd-TiO_2 in the UV light region was apparently higher than that in the visible light region, according to the DRS analytics result of Nd-TiO_2 nanoparticles. However, performing removal of different VOCs was different. This may be caused by two reasons: 1) the compatibility between VOCs and [HMIm]PF_6 ionic liquid might have facilitated the enrichment of VOCs on the surface of SILM and the dissolution of VOCs in [HMIm]PF_6 ionic liquid [36]; 2) the decomposition of VOC molecules depends on the complexity of electronic and spatial structure of VOC molecules.

Fig. 10 shows the degradation rate and rate of removal of toluene, acetone, chloroform, benzene, and xylene by [HMIm]PF_6/Nd-TiO_2 SILM under UV light and visible light illumination for 10 h. Owing to the synergy between the membrane separation process and the photocatalysis, the VOC removal rate was higher than 70.0% and 60.0% under UV light and visible light, respectively, in which only a part of the VOCs could be degraded to nontoxic CO_2 and H_2O. The concentration of VOCs was measured at the outlet of the membrane module; the degradation rate of toluene, acetone, chloroform, benzene, and xylene was 43.94%, 52.76%, 51.72%, 51.67%, and 39.32% under UV light illumination, and 28.28%, 39.43%, 39.82%, 39.07%, and 28.77% under visible light illumination, respectively.

Whether the SILMs can be practically applied depends on its stability. In this study, the amount of permeated air and the permeate side pressure were determined during the operation, which was evaluated as the lifetime of the SILM. The flow rate of permeated air and permeate side pressure were usually 1.8–5.0 cm^3/min and 1.5–2.2 kPa, respectively when the flow rate of sweep air was 0. When the operation time of [HMIm]PF_6/Nd-TiO_2 SILM was over 1000 h, the stability of SILM did not vary.

3.3. Removal mechanism

The catalytic membrane-based mechanism diagram of VOC removal through [HMIm]PF_6/Nd-TiO_2 SILM under UV light and visible light illumination is shown in Fig. 11. Gaseous VOCs will be concentrated on the membrane surface under the effect of the difference of partial pressure. Subsequently, a portion of the VOCs dissolves in the [HMIm]PF_6 ionic liquid according to the similarity-compatible principle and then diffuses through the ionic liquid membrane, and the ionic liquid can be dissociated and reused. Meanwhile, most of concentrated VOCs can be degraded to CO_2 and H_2O by the photocatalytic effect of Nd-TiO_2 nanoparticles under UV–Vis light, and the degradation products permeate though the ionic liquid membrane. With the photocatalyst Nd-TiO_2 nanoparticles, Nd acts as an electron by supplying ions electrons to TiO_2, and the photogenerated electrons react with O_2 to form O_2^-radicals, whereas the photogenerated holes react with water to produce •OH radicals, which also can degrade VOCs. This synergistic effect can facilitate VOC removal.

4. Conclusion

A SILM with photocatalytic function containing 1-hexyl-3-methylimidazolium hexafluorophosphate ionic liquid and synthesized Nd-TiO_2 nanoparticles was devised. The as-prepared photocatalytic SILM under UV and visible light illumination was effective for VOC removal to improve air quality. The VOC concentration in the chamber (1000 ppm of toluene, acetone, chloroform, benzene, and xylene) could be reduced to a lower level of less than 200~400 ppm over 10 h of operation time. Performing VOC removal was illustrated in terms of the synergistic effect of membrane separation and photocatalytic reaction, and the VOC removal mechanism of the catalytic membrane-based reactor was presented. We conclude this SILM containing photocatalytic nanoparticles under UV–Vis light illumination can provide a highly efficient and environment friendly method for removing VOCs. mmc1.docx

Declaration of Competing Interest

There is no conflict of interest.

CRediT authorship contribution statement

Boxin Li: Writing - original draft. **Guozhe Sui:** Conceptualization, Data curation, Resources. **Lijuan Du:** Writing - review & editing, Data curation. **Yan Zhuang:** Data curation, Resources. **Yulin Zhang:** Data curation, Investigation. **Yuanfang Zou:** Writing - review & editing.

Acknowledgments

This work was supported by the Research Project of Education Ministry of Heilongjiang Province of China (135209217, 135409101). We would like to thank Editage (www.editage.cn) for English language editing.

References

[1] W.X. Zou, B. Gao, Y.S. Ok, L. Dong, Integrated adsorption and photocatalytic degradation of volatile organic compounds (VOCs) using carbon-based nanocomposites: a critical review, Chemosphere 218 (2019) 845–859, doi:10.1016/j.chemosphere.2018.11.175.

[2] X.Y. Zhang, B. Gao, A.E. Creamer, C.C. Cao, Y.C. Li, Adsorption of VOCs onto engineered carbon materials: a review, J. Hazard. Mater. 338 (2017) 102–123, doi:10.1016/j.jhazmat.2017.05.013.

[3] Y. Naciri, A. Hsini, Z. Ajmal, J.A. Navio, B. Bakiz, A. Albourine, M. Ezahri, A. Benlhachemi, Recent progress on the enhancement of photocatalytic properties of BiPO4 using pi-conjugated materials, Adv Colloid Interface Sci 280 (2020) 102160, doi:10.1016/j.cis.2020.102160.

[4] H. Nigar, N. Navascues, O. de la Iglesia, R. Mallada, J. Santamaria, Removal of VOCs at trace concentration levels from humid air by microwave swing adsorption, kinetics and proper sorbent selection, Sep Purif Technol 151 (2015) 193–200, doi:10.1016/j.seppur.2015.07.019.

[5] G.Z. Sui, J.L. Li, L.J. Du, Y. Zhuang, Y.L. Zhang, Y.F. Zou, B.X. Li, Preparation and characterization of g-C3N4/Ag–TiO2 ternary hollowsphere nanoheterojunction catalyst with high visible light photocatalytic performance, J Alloys Compd 283 (2020) 153851, doi:10.1016/j.jallcom.2020.153851.

[6] O. Debono, V. Hequet, L.Le Coq, N. Locoge, F. Thevenet, VOC ternary mixture effect on ppb level photocatalytic oxidation: removal kinetic, reaction intermediates and mineralization, Appl Catal B–Environ 218 (2017) 359–369, doi:10.1016/j.apcatb.2017.06.070.

[7] L.Y. Wang, H. Xu, J.K. Gao, J.M. Yao, Q.C. Zhang, Recent progress in metal-organic frameworks-based hydrogels and aerogels and their applications, Coord Chem Rev 398 (2019) 213016, doi:10.1016/j.ccr.2019.213016.

[8] C. Wang, Y.H. Ao, P.F. Wang, J. Hou, J. Qian, Preparation of cerium and nitrogen co-doped titania hollow spheres with enhanced visible light photocatalytic performance, Powder Technol 210 (2011) 203–207, doi:10.1016/j.powtec.2011.03.015.

[9] Y. Wang, Y. Wang, Y.L. Meng, H.M. Ding, Y.K. Shan, X. Zhao, X.Z. Tang, A highly efficient visible-light-activated photocatalyst based on bismuth- and sulfur-codoped TiO2, J Phys Chem C 112 (2008) 6620–6626, doi:10.1021/jp7110007.

[10] C. Lei, J.K. Gao, W.J. Ren, Y.B. Xie, S.Y.H. Abdalkarim, S.L. Wang, Q.Q. Ni, J.M. Yao, Fabrication of metal-organic frameworks@cellulose aerogels composite materials for removal of heavy metal ions in water, Carbohydr Polym 205 (2019) 35–41, doi:10.1016/j.carbpol.2018.10.029.

[11] F. Soumya, N. Yassine, H. Abdelghani, B. Hanane, B. Asmae, A. Abdallah, N. Abderrazak, G. Taoufiq, Evolution of the physicochemical and photocatalytic properties of BaO embedded in bismuth phosphovanadates glasses, Chem Phys Lett 763 (2021) 138173, doi:10.1016/j.cplett.2020.138173.

[12] J.L. Li, S.Q. Jia, G.Z. Sui, L.J. Du, B.X. Li, Preparation of hollow Nd/TiO2 sub-microspheres with enhanced visible-light photocatalytic activity, RSC Adv 7 (2017) 34857–34865, doi:10.1039/c7ra05228f.

[13] U. Alam, T.A. Shah, A. Khan, M. Muneer, One-pot ultrasonic assisted sol-gel synthesis of spindle-like Nd and V codoped ZnO for efficient photocatalytic degradation of organic pollutants, Sep Purif Technol 212 (2019) 427–437, doi:10.1016/j.seppur.2018.11.048.

[14] S. Wang, Z.Y. Wang, Y. Wang, C.H. Xia, E. Hong, L.M. Bai, T. Li, B.Q. Wang, Study on the controlled synthesis and photocatalytic performance of rare earth Nd deposited on mesoporous TiO2 photocatalysts, Sci Total Environ 652 (2019) 85–92, doi:10.1016/j.scitotenv.2018.10.154.

[15] R. Kralchevska, M. Milanova, T. Tisler, A. Pintar, G. Tyuliev, D. Todorovsky, Photocatalytic degradation of the herbicide iodosulfuron by neodymium or nitrogen doped TiO2, Mater Chem Phys 133 (2012) 1116–1126, doi:10.1016/j.matchemphys.2012.02.025.

[16] C. Castel, E. Favre, Membrane separations and energy efficiency, J Memb Sci 548 (2018) 345–357, doi:10.1016/j.memsci.2017.11.035.

[17] M. Diaz, A. Ortiz, I. Ortiz, Progress in the use of ionic liquids as electrolyte membranes in fuel cells, J Memb Sci 469 (2014) 379–396, doi:10.1016/j.memsci.2014.06.033.

[18] A. Faghihi-Zarandi, H. Shirkhanloo, C. Jamshidzadeh, A new method for removal of hazardous toluene vapor from air based on ionic liquid-phase adsorbent, Int J Environ Sci Te 6 (2018) 2797–2808, doi:10.1007/s13762-018-1975-5.

[19] J.F. Wang, J.Q. Luo, S.C. Feng, H.R. Li, Y.H. Wan, X.P. Zhang, Recent development of ionic liquid membranes, Green Energy Environ 1 (2016) 47–65, doi:10.1016/j.gee.2016.05.002.

[20] T. Uragami, Y. Matsuoka, T. Miyata, Permeation and separation characteristics in removal of dilute volatile organic compounds from aqueous solutions through copolymer membranes consisted of poly(styrene) and poly(dimethylsiloxane) containing a hydrophobic ionic liquid by pervaporation, J Memb Sci 506 (2016) 109–118, doi:10.1016/j.memsci.2016.01.031.

[21] A. Dahi, K. Fatyeyeva, D. Langevin, C. Chappey, S.P. Rogalsky, O.P. Tarasyuk, A. Benamor, S. Marais, Supported ionic liquid membranes for water and volatile organic compounds separation: sorption and permeation properties, J Memb Sci 458 (2014) 164–178, doi:10.1016/j.memsci.2014.01.031.

[22] J.L. Li, T.T. Zhao, G.Z. Sui, S.Q. Jia, CO2 separation from air using microporous polyvinylidene fluoride-supported triethylene glycol/alkanolamine liquid membranes, Mater Express 6 (2016) 183–190, doi:10.1166/mex.2016.1291.

[23] T.L.R. Hewer, E.C.C. Souza, T.S. Martins, E.N.S. Muccillo, R.S. Freire, Influence of neodymium ions on photocatalytic activity of TiO2 synthesized by sol–gel and precipitation methods, J Mol Catal A–Chem 336 (2011) 58–63, doi:10.1016/j.molcata.2010.12.010.

[24] F. Ruggieri, A.A. D'Archivio, M. Fanelli, S. Santucci, Photocatalytic degradation of linuron in aqueous suspensions of TiO2, RSC Adv 1 (2011) 611–618, doi:10.1039/c1ra00133g.

[25] S. Ida, P. Wilson, B. Neppolian, M. Sathish, P. Karthik, P. Ravi, Ultrasonically aided Selective Stabilization of Pyrrolic type nitrogen by one pot nitrogen doped and hydrothermally reduced Graphene oxide/Titania nanocomposite (N-TiO2/N-RGO) for H-2 production, Ultrason Sonochem 57 (2019) 62–72, doi:10.1016/j.ultsonch.2019.04.041.

[26] A. Bokare, M. Pai, A.A. Athawale, Surface modified Nd doped TiO2 nanoparticles as photocatalysts in UV and solar light irradiation, Sol Energy 91 (2013) 111–119, doi:10.1016/j.solener.2013.02.005.

[27] D.F. Sun, K. Wang, Z.J. Xu, R.X. Li, Synthesis and photocatalytic activity of sulfate modified Nd-doped TiO2 under visible light irradiation, J Rare Earth 33 (2015) 491–497, doi:10.1016/S1002-0721(14)60446-4.

[28] A. Ray, A. Roy, P. Sadhukhan, S.R. Chowdhury, P. Maji, S.K. Bhattacharya, S. Das, Electrochemical properties of TiO2-V2O5, nanocomposites as a high performance supercapacitors electrode material, Appl Surf Sci 433 (2018) 581–591, doi:10.1016/j.apsusc.2018.02.277.

[29] N.R. Khalid, E. Ahmed, Z.L. Hong, Y.W. Zhang, M. Ullah, M. Ahmed, Graphene modified Nd/TiO2 photocatalyst for methyl orange degradation under visible light irradiation, Ceram Int 39 (2013) 3569–3575, doi:10.1016/j.ceramint.2012.10.183.

[30] J. Du, X. Gu, Q. Wu, J. Liu, H.Z. Guo, J.G. Zou, Hydrophilic and photocatalytic activities of Nd-doped titanium dioxide thin films, Trans Nonferrous Met Soc China 25 (2015) 2601–2607, doi:10.1016/S1003-6326(15)63881-X.

[31] X.L. Wang, H.Y. Yin, Q.L. Nie, W.W. Wu, Y. Zhang, L.Y. Qiu, Hierarchical Ag/AgCl-TiO2 hollow spheres with enhanced visible-light photocatalytic activity, Mater Chem Phys 185 (2017) 143–151, doi:10.1016/j.matchemphys.2016.10.017.

[32] Y. Chen, Q. Wu, C. Zhou, Q.T. Jin, Enhanced photocatalytic activity of La and N co-doped TiO2 /diatomite composite, Powder Technol 322 (2017) 296–300, doi:10.1016/j.powtec.2017.09.026.

[33] Z.S. Wei, L. Rosa, K.L. Wang, M. Endo, S. Juodkazis, B. Ohtani, E. Kowalska, Size-controlled gold nanoparticles on octahedral anatase particles as efficient plasmonic photocatalyst, Appl Catal B–Environ 206 (2017) 393–405, doi:10.1016/j.apcatb.2017.01.043.

[34] S.Q. Jia, J.L. Li, G.Z. Sui, L.J. Du, Y.L. Zhang, Y. Zhuang, B.X. Li, Synthesis of 3D flower-like structured Gd/TiO2@rGO nanocomposites via a hydrothermal method with enhanced visible-light photocatalytic activity, RSC Adv 9 (2019) 31177–31185, doi:10.1039/c9ra06045f.

[35] Y.M. Wu, J.L. Zhang, L. Xiao, F. Chen, Properties of carbon and iron modified TiO2 photocatalyst synthesized at low temperature and photodegradation of acid orange 7 under visible light, Appl Surf Sci 256 (2010) 4260–4268, doi:10.1016/j.apsusc.2010.02.012.

[36] G.Z. Sui, J.L. Li, A. Ito, Separation of VOC vapor from air by a surface-soaked liquid membrane module using triethylene glycol, Sep Purif Technol 68 (2009) 283–287, doi:10.1016/j.seppur.2009.05.006.